Metals and Materials International (2021) 27:456–466
https://doi.org/10.1007/s12540-020-00795-6

Influence of Phase Composition in TiAlSiN Hard Coatings on the Evolution of Structure and Mechanical Properties

Jeong-Han Lee[1,2] · Ik-Hyun Oh[1] · Jun-Ho Jang[1] · Ju-Hun Kim[1,2] · Sung-Kil Hong[2] · Hyun-Kuk Park[1]

Received: 19 May 2020 / Accepted: 15 June 2020 / Published online: 9 July 2020

Abstract
The aim of this study is to investigate the structural evolution and mechanical properties of TiAlSiN coatings when processed by the arc ion plating method. To form a hard coating, Ti, Al, and Si powders were mechanically alloyed by planetary ball milling; the powders were then densely compacted during a rapid sintering process into a ternary system coating, i.e. TiAlSi. The evolution of the structural phase from a powder to a compact material is dominated considerably by phase states such as a supersaturated solid solution or intermetallic compounds. In the case of coating layers, the factors that determine the structural evolution are associated with the phase stability of the nano-crystalline structure that in turn is associated with the Ti/Al composition ratio. Motivated by this, we performed experiments to investigate the distribution of microstructures; the material's binding energy, quantitative properties, transformation of crystal structure, and distribution of amorphous/crystalline were all recorded. In particular, the relationship between the physical and chemical properties during the coating process is considered to be the dominant factor controlling the orientation and morphology of that zone (1, T, and 2). The TiAlSiN coating layer was found to have hardness above 45 GPa and an adhesion above 100 N. In other words, understanding the evolution and structure of TiAlSin helped us to produce a material with excellent properties that can be used as a hard coating. Specifically, these properties were induced by a grain refinement of the nano-crystalline structure that corresponds to an increase in the silicon nitride contents.

Keywords TiAlSiN · Hard coating · Nitride nano-composites · Crystal structure · Mechanical properties

1 Introduction

The trend in hard coating materials for cutting tools has been to develop stacking binary, ternary or quaternary nitrides, and to even use multiple-composite coatings starting with the nitrides of single metals based mainly on transition metal nitrides [1–4]. Recently, high-performance (i.e. a high strength, heat resistance, and adhesion, oxidation and wear resistance with a low friction coefficient) coating layers fabricated using the nanonization of nitrides have been reported in several papers [5–10]. In particular, TiN-based coating materials have been receiving attention due to their excellent wear and corrosion resistance, they are also thought of as a representative transition metal nitride (MX(N), M: transition metal, X: additional elements, N: nitride). Unfortunately, their tool life is limited due to severe oxidation and wears at temperatures over 500 °C [11, 12].

In order to improve their hardness and oxidation resistance researchers have been looking at ternary coating layers by adding Al or Si to produce coatings resistant to high temperatures and speeds [2, 13, 14]. Notably, when Al is substituted in the lattice of TiN [15, 16], a solid solution of TiAlN forms stress fields within a bct (body centered tetragonal) structure, contributing to a strengthening of the solid solution [17]. In addition, as the temperature is raised Al atoms have a tendency to oxidize to form an Al_2O_3 layer, however, with TiAlN this can be withstood up to 1100 °C [18, 19]. TiSiN, with Si added to TiN, has been reported [20–22] to increase hardness and high temperature stability, these improvements are induced by controlling grain growth and cohesive energy [20, 21] at the interface of the crystalline/amorphous structures, such as when Si_3N_4 is formed

✉ Hyun-Kuk Park
hk-park@kitech.re.kr

[1] EV&Components Materials Group, Korea Institute of Industrial Technology (KITECH), Gwangju 61012, Republic of Korea

[2] Materials Science and Engineering, Chonnam National University, Gwangju 61186, Republic of Korea

in the coating microstructure [23], this gives a hardness of more than 40 GPa and an oxidation resistance of more than 950 °C. On the other hand, when the Si content exceeds a certain amount (> 20 at%) a non-nitride rich Si phase is precipitated in the coating texture, causing a decrease in the hardness and homogeneity of the columnar structures with poor density [24, 25]. With these efforts, TiAlSiN coatings have reached a level that ensures desirable physical properties when used with cutting tools. Several studies have reported [26–28] that controlling parameters (e.g. bias, arc powder, temperature, and flow rate of N_2 gas, etc.) in the coating process the microstructural evolution and driving force (e.g. ion bombardment and kinetic energy) in the coating layer also ensures a long tool life. In addition, there have been investigations [29–31] into the structural behavior during the phase transformation the from the target materials into the TiAlSiN coatings, in particular, researchers have looked at the composition ratio of Ti/Al and the quantitative distribution between Si_3N_4 amorphous and nitride crystalline structures. Furthermore, these approaches have provided lattice parameters for TiAlSiN as a function of the Al and Si contents; as such these dependencies can be used for estimating the amount of alloying elements in the respective phases.

Consequently, in order to clarify the experimental evidence mentioned above, in this study, we take several approaches: (1) we examine the structural evolution and how to maintain phase stability from alloyed powder and compacts (=target materials) to the coating layer, i.e. from supersaturated solid solution to an intermetallic composite, (2) we investigate the quantitative distribution according to chemical bond and binding energy in the TiAlSiN coating layer, (3) By varying the lattice parameters of the nitride crystalline we look at its microstructural evolution, and (4) We discover the effect of varying the amorphous phase contents on the coating's mechanical properties, i.e. the behavior of Si_3N_4. These tests were conducted by means of XRD, XPS, TEM, and 3D-implementation.

2 Experimental

The initial powders are of more than 99.95% purity Ti (Ave. 28.5 μm), Al (Ave. 9.1 μm), and Si (Ave. 20.0 μm), these were mechanically alloyed by planetary ball milling after mixing in accordance with the designed compositions, i.e. $Ti_{50}Al_{45}Si_5$ (#1), $Ti_{45}Al_{45}Si_{10}$ (#2), and $Ti_{40}Al_{45}Si_{15}$ (#3). The milling process lasted for 24 h to ensure phase transformations from intermetallic compounds to supersaturate even amorphous phases. In addition, at the milling speed 300 RPM, PCA was added ethanol (4 wt%), the ratio of stainless steel ball to powders was set to 15:1 in the vial. In order to fabricate a dense, compact material, the coating target along with the TiAlSi ternary materials were consolidated by a rapid sintering process with the temperature at 1000 °C under 60 MPa pressure under 60 °C/min heating rate over 17 min.

The TiAlSiN coatings were deposited by an AIP system with densely consolidated TiAlSi compacts as the target material and cemented carbide (WC-3 wt%Co) as the substrate. Deposition was carried out using a bias voltage of -60 V, an arc power 100 A, and substrate temperature of 450 °C, coatings were synthesized with nitride by means of N_2 gas (flow rate of 20 sccm) with a pressure of 5×10^{-6} torr after glow discharge of Ar gas.

The chemical bonding states of the coating materials were investigated by XPS analysis with Al-Kα radiation (1486.6 eV). We used Thermofisher software for calibration and alignment of the XPS spectra, the quantitative distribution of the nitride composites (e.g. with crystalline or amorphous) can be fitted with a Gaussian function using Eq. (1).

$$y = y_0 + \frac{A}{w\sqrt{\pi/2}} e^{-2\frac{(x-x_c)^2}{w^2}} \tag{1}$$

In Eq. (1), A is the area under the Gaussian curve, x_c is the coordinate at the center, w is the width of the peak corresponding to $w = 2\sigma$, and σ is the error parameter for the Gaussian area [13].

The grain size and micro-strain of the nitride crystalline structure in the TiAlSiN coatings was measured by a Williamson-Hall plot [32], following consideration of Debye–Scherrer's formula [32] using the XRD (PIXCEL 1D DETECTOR, Panalytical) patterns:

$$D = \frac{k\lambda}{\beta_{hkl}\cos\theta}, \quad \varepsilon = \frac{\beta_{hkl}}{4\tan\theta} \tag{2}$$

$$\beta_{hkl} = \left(\frac{k\lambda}{D\cos\theta}\right) + 4\varepsilon\tan\theta \tag{3}$$

$$\beta_{hkl}\cos\theta = \left(\frac{k\lambda}{D}\right) + 4\varepsilon\sin\theta \tag{4}$$

The average of nanocrystalline size and strain from crystal distortion as well as imperfections were calculated using Eq. (2). Here, D is the crystalline size, the shape factor, k, is 0.9, and λ is the wavelength of CuKα radiation. When the size and strain contributions to peak broadening are independent of each other, the observed profile is simply the sum of Eqs. (3) and (4).

To explore our samples' structural evolution based on their lattice information from alloyed powder to compacts to coatings, the materials were analyzed by XRD and their patterns were checked for any peak shifting or broadening, which was then compared to the corresponding phase

state's indexing information. Furthermore, the results were processed by the High-Score Plus application in order to match the JCPDS card. A visual representation of the lattice structure's evolution was created based on the refined XRD data using the VESTA software [33].

The microstructures of the TiAlSiN coating layers were observed using TEM analysis (JEM-2100F HR, JEOL Ltd.) after the samples had been milled with the FIB system (Helios NanoLab™, FEI). Looking at the HR images and their XRD patterns, we attempted to identify the samples using their inherent lattice parameters and the distribution of nitride crystalline structure.

Three mechanical properties were measured. First, the hardness of the coatings were measured by a micro Vickers hardness tester with a load of 20 g for 15 s; the length of the indentation that was made was converting to $Hv_{0.02}$ using Eq. (5) [34].

$$Hv = 2P\sin\frac{\frac{\alpha}{2}}{d^2} = 1.8544P/d^2 \tag{5}$$

where P is the load (F) of applied force, d is the diagonal of the impression with indentation, and α is the face angle of the diamond at 136°.

Second, the adhesion of coatings were analyzed using a scratch tester instrument (REVETEST, CSM) with a load from 1 to 200 N while checking for fracture (critical load; L_{c1}, L_{c2}, and L_{c3}) using Eq. (6) [35].

$$L_{CN} = \left(L_{rate} \times \left(\frac{I_N}{X_{rate}}\right)\right) + L_{strat} \tag{6}$$

where L_{CN} is critical scratch load, L_{rate} is load speed, I_N is the distance from the start point to the point where the Nth event occurred, X_{rate} is scratch displacement rate, and L_{strat} is load at the start of the scratch.

Third, the roughness (RMS, R_q) and micro morphology were calculated by film figure analyzer (Contour GTK-A, Bruker).

3 Results and Discussion

Figure 1 shows the structural evolution showed with XRD patterns from alloyed powder to compact to coating layer of each composition. In the initial alloy design, it has been confirmed that the different crystalline structures that can occur depend on the Ti/Al ratio. The crystallinity of the TiAlN or AlTiN intermetallic nitrides is related to their phase stability [36–38]. The phase stabilities of the supersaturated solids were determined not only by their stoichiometry but also by their Al phase distribution in the sublattice. In this case, molar ratio of AlN inside TiN lattice is 0.40–0.91 for crystallization of TiAlN [38]. The decrease in the number of Ti–Al bonds in the lattice may increase the metastable solubility limit of AlN in TiAlN, it can be explained that in terms of Ti–Al binding energy affected that the solubility limit depends largely on energy relation, i.e. formation of energy difference (ΔE_f) and constituent entropy.

The energy difference (ΔE_f) is a chemical driving force capable of decomposing TiN and AlN, a larger driving force must be generated in order to decompose TiAlN into TiN and AlN. In other words, the number of Ti–Al bonds could be increased. The TiAlN lattice has a high degree of super saturation (see the Fig. 1c, ◈: Ti(Al, Si) s.s.s), its crystallinity decreases due to an increase in the limit of metastable solubility in the lattice, which was behavior of crystallization due to the decrease of constituent entropy was suppressed, i.e. compare Fig. 1a, b, see the peaks of (002) plane indexing the $TiAlN_2$. Figure 1c of the Al-rich composition (45 at%) of relatively, the peak intensity decreased locally. Because of expected to be due to the increased distribution

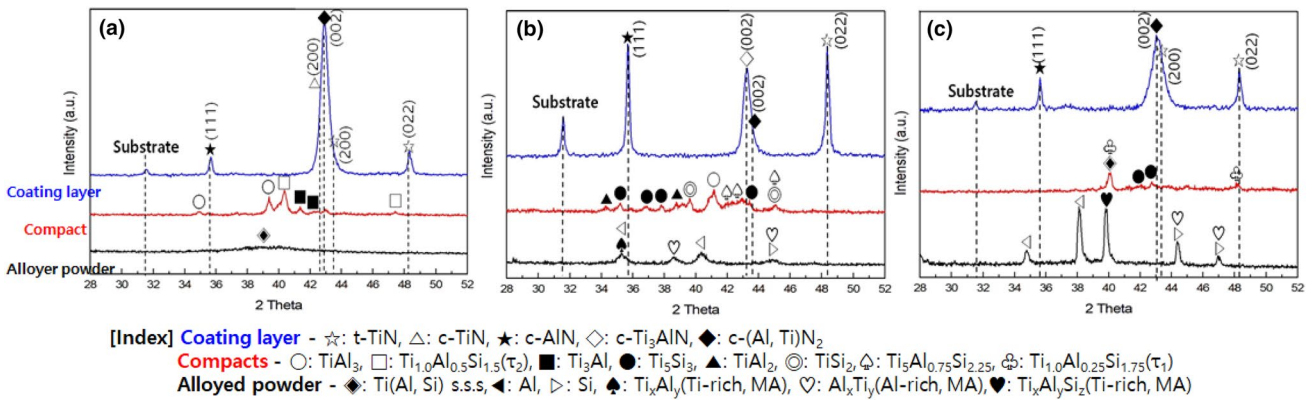

Fig. 1 XRD patterns of the as-deposited TiAlSiN coating layers with various composition ratios: **a** $Ti_{50}Al_{45}Si_5N$, **b** $Ti_{45}Al_{45}Si_{10}N$, and **c** $Ti_{40}Al_{45}Si_{15}$

of crystalline/amorphous mixed phases due to inducing with formation of Si_3N_4 according to the high content of Si. The reduction of crystallinity of TiAlN or AlTiN were estimated near the (42–44)°, which was indicating a peak broadening.

Consequently, variation in the metastable solubility and the degree of bonds during the evolution of powder to compact affected the phase constituent of nitrides in coating layer. For instance, in the phase constituent of coating layer, it can be seen at Fig. 1a that the formation of c-(Al, Ti)N_2 formed by supersaturation AlN into TiN lattice with a initially saturated from powder can be constructed. Contrary, in Fig. 1b hardly saturated as intermetallic compounds from powder to compacts, which were promoted to c-Ti_3AlN nitride.

Figure 2 presents the XPS spectra that show the presence of Ti–N, Al–N, Ti–Al–N, and Si–N chemical bonds in deposited coatings. Deconvolution of the Al 2*p* (see the Fig. 2b) and N 1*s* (see the Fig. 2d) peaks show that the TiAlSiN film is made of three components. The Ti 2*p* spectra in Fig. 2a show there are two components in the nitride crystalline, with binding energies except for unfulfilled nitride of single phase in Ti 2*p* 1/2 (e.g. metallic phase-Ti at the 463.5 eV). The present Ti–N corresponds to the peaks at 456.3, 457.6, and 461.3 eV. The presence of another nitride, Ti–Al–N, was indicated by the peak at 455.2 eV. Looking at the Al 2*p* spectra in Fig. 2b, the Ti–Al bonds in the complex nitride are shown by peaks in the range of (73.5–75.0) eV. Al–N corresponds to 74.2 eV, the peak intensity here clearly points to an Al-rich composition. The presence of the Ti–Al–N complex nitride is indicated by peaks at two binding energies, 73.5 and 75.0 eV, these structures can be classified by their phase stability, which corresponds to the number of Ti–Al bonds present, the variation of peak intensity points to the phase stability of the sample. For the Si 2*p* spectra in Fig. 2c, the Si–N bonds thought to be in an amorphous phase were distributed at different binding

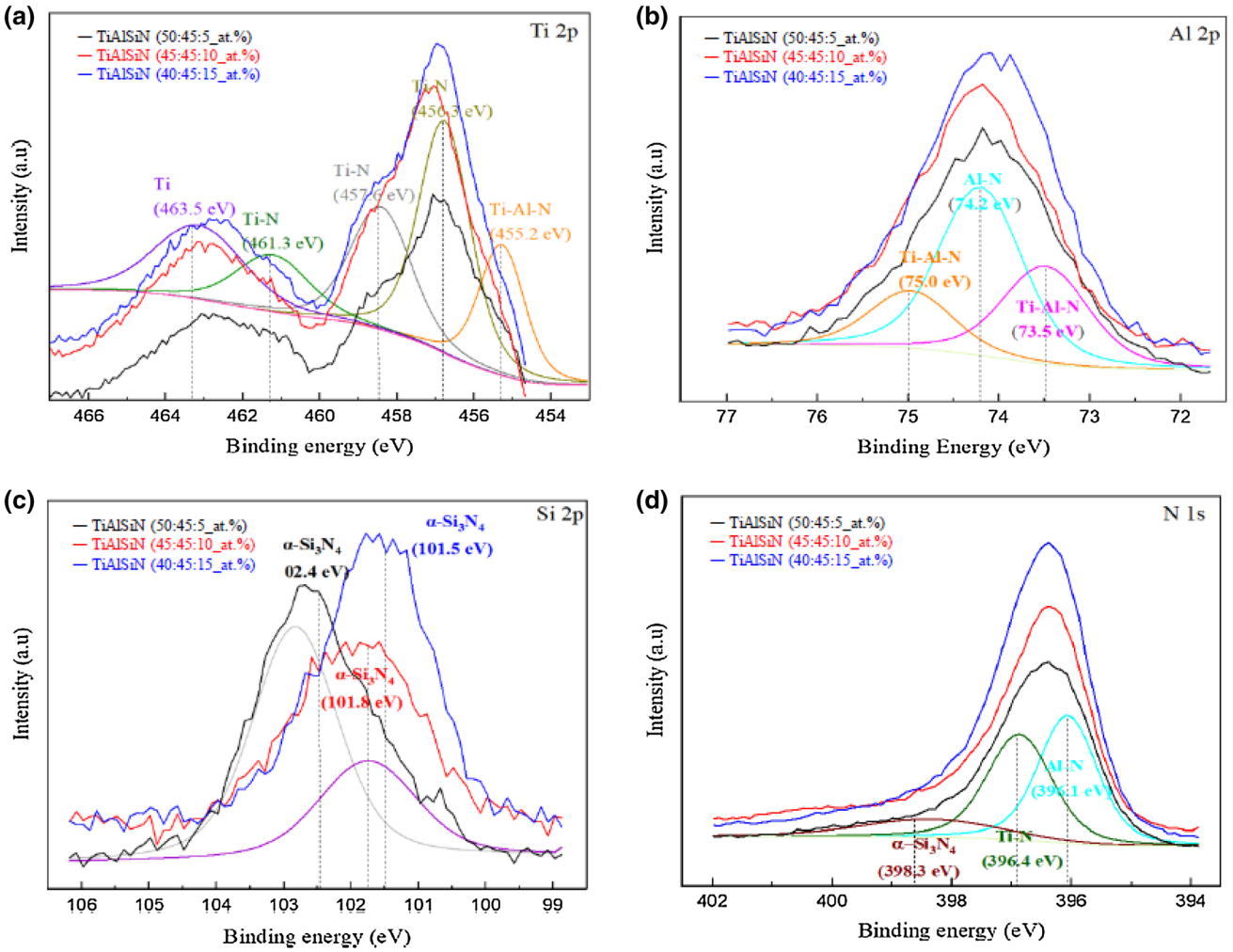

Fig. 2 XPS spectra of TiAlSiN coating layers with various composition ratios: **a** Ti 2*p*, **b** Al 2*p*, **c** Si 2*p*, and **d** N 1*s*

energies so the peak appeared in the range of (101.5–102.4) eV [39–41], whereas the presence of free Si (indicated by a peak at 99.28 eV [42]) was hardly detected due to the high ionization rate under nitrogen flow during the AIP process, this is reasonable evidence for the formation of Si_3N_4.

The binding energies of Si_3N_4 vary according to the Ti/Al composition ratio, the reason for a difference in binding energies in the case of the Si_3N_4 in Fig. 2c could be estimated to the two major factors interact. The affect of bonding strength (E_{Ti-Si}) during the ionization from compacts by the phase stability of contained titanium-silicide components of nearest neighbor atoms in the perfect tetrahedral (e.g. Si-SiSiN) [43] could be considered. Differences in phase stability are closely related to thermodynamic aspects of the Gibbs free energy [44] in Ti_xSi_y intermetallic compounds or Ti(Al, Si) solid solution (metastable), the formation energy of an intermetallic is lower than a supersaturated solid solution, this corresponds to higher phase stability, i.e. $E^1_{Ti-Si} > E^2_{Ti-Si} > E^3_{Ti-Si}$, where E: bonding strength (kJ/mol), E^1: Ti_xSi_y binary intermetallic (see the Fig. 1b, ●: Ti_5Si_3, ◎: $TiSi_2$), E^2: $Ti_xAl_ySi_z$ ternary intermetallic (see the Fig. 1c, ♧: $Ti_{1.0}Al_{0.25}Si_{1.75}(\tau_1)$), E^3: supersaturated solid solution (see the Fig. 1c, ◈: Ti(Al, Si) s.s.s). Thus, it is estimated that stoichiometrically stable intermetallic compounds could suppress the formation of stable tetrahedral silicon nitride in the coating layer while maintaining a relatively strong bonding energy (e.g. Ti_5Si_3: 1095.0 kJ/mol, and $TiSi_2$: 116.7 kJ/mol) during the ionization process, which induces non-stoichmetrical silicon nitrides (e.g. Overlapping Si_3N_4 detected as Si_3N_4/Si [at 101.8 eV (see #2)] and $SiN_{0.91}$ [at 101.5 eV (see #3)], respectively). The standard error for all spectra measurements is within ± 0.1 eV.

Figure 3 shows relative contribution of bonds within the nitrides through CPS.eV (counts per second per electron-volt) area of the XPS spectra in Fig. 2. The nitride distributions (see the vol%), calculated using quantifying data, are exhibited (see Fig. 3a–c) according to the composition ratio. The distribution of nitrides is affected by the configuration of $Ti_xAl_ySi_z$. In Fig. 3a, the Ti-rich corner could promote the formation of TiN instead of other compositions, the distribution of TiN is approximately 24.9 vol%. Its distribution was boosted due to the formation of non-distorted cubic structured TiN nitrides that are relatively unaffected by being near the stress field upon configured of nitrides. The result of Fig. 1a shows that c-TiN in the (200) plane was detected without forming a (Al, Ti)N_2 solid solution. Figure 3b, the increase in the distribution of intermetallic nitrides (e.g. Ti_3AlN) is noticeable. The Al/(Ti + Al) composition ratio (x = 0.50, #2) may indicate the preferential formation of MN(X)-based transition metal nitrides at maximum solid solubility without transformation of the crystalline structure. In other compositions, (x = 0.47, #1) could be caused to configure supersaturated solid solution, however (x = 0.53, #3) was considered that in excess of the critical composition of the crystal structure transition, which was indicated that in the metastable phases c-AlN substituted in TiN could be transformed into h-AlN of precipitated finely. Contrary to the behavior of these intermetallic compounds, amorphous nitrides like Si_3N_4 could form locally to decrease phase stability at the interface with the nearby intermetallic nitrides. The Si-rich composition in Fig. 3c has a large volumetric distribution (37.9 vol%) of Si_3N_4. In addition, as shown in Fig. 4, there is a peak shifting and intensity decrease due to a transition in lattice structure (e.g. (Al, Ti)$N_2 \rightarrow Ti_3AlN$) that occurs at the same time as an increase of Si content.

Figure 5 shows the micrographs of the $Ti_{50}Al_{45}Si_5$ (#1) coating layer. Figure 5a, shows the thickness of the coating layer deposited is about 3.4 μm, it consists of several zones: 1, T, 2. In addition, Fig. 5b shows an enlarged BF image of the amorphous/columnar structures (in zone 2) with their diffraction patterns. In A region it was observed in the SAED patterns that the structure is preferentially oriented to the (111) and (012) planes, this indicates a dense nano crystalline area that seems to be consistent with typical overlapping patterns. Furthermore, in B region there is mixed phase at the Si_3N_4/crystalline interface, this is known as a diffused ring pattern [45]. Notably, Fig. 5c clearly shows the presence of two-sublattices (see FFT image in C region), evidence for the co-existent t-TiN

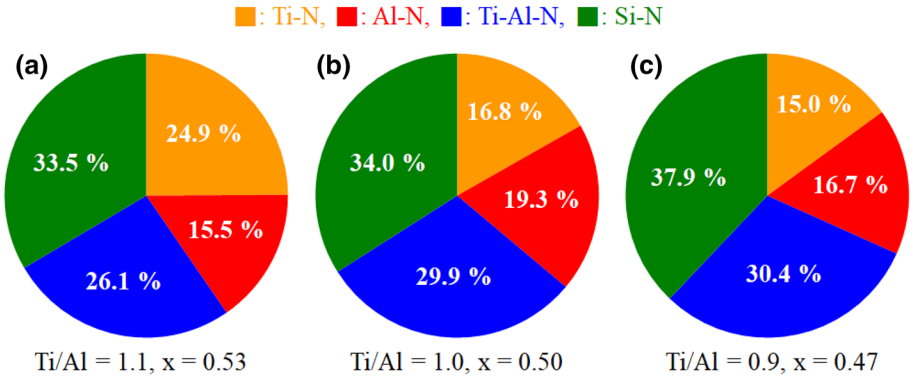

Fig. 3 The relative contribution (vol%) of bonds in the TiAlSiN coatings with different Ti/Al ratios fitted using XPS spectra peaks: **a** $Ti_{50}Al_{45}Si_5N$ (#1), **b** $Ti_{45}Al_{45}Si_{10}N$ (#2), and **c** $Ti_{40}Al_{45}Si_{15}$ (#3)

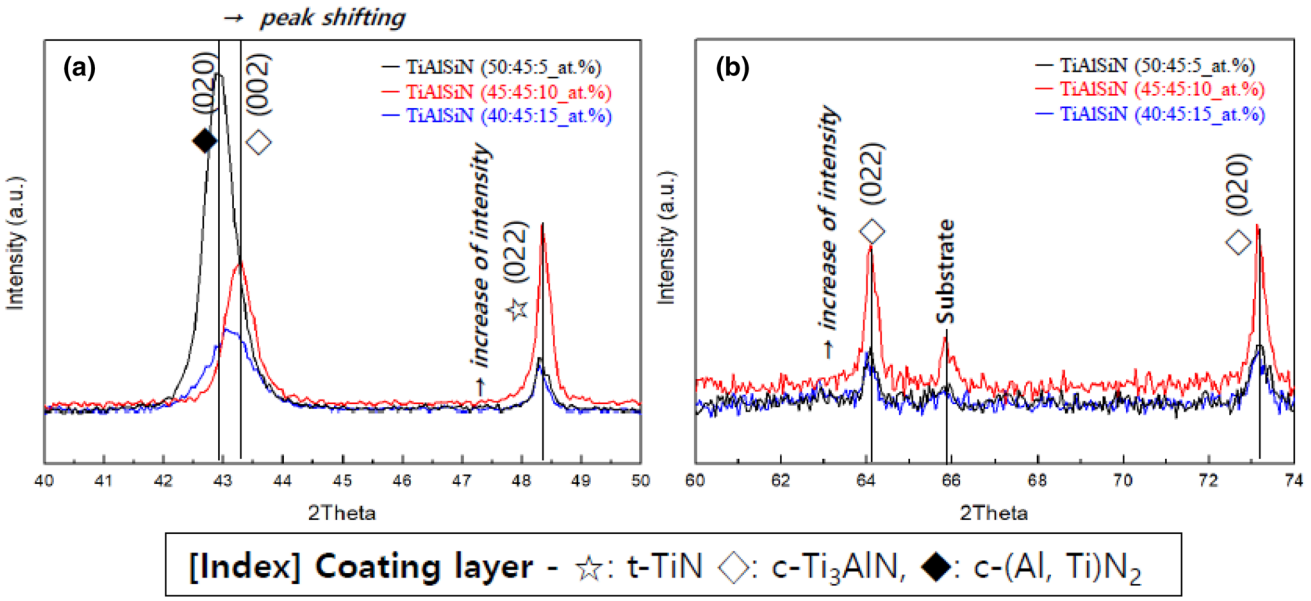

Fig. 4 Representative enlarged (from Fig. 1) XRD spectra of the as-deposited TiAlSiN coating layers, corresponding to specific 2 theta range with variation of peak morphology: **a** (40~50)°, and **b** (60~74)°

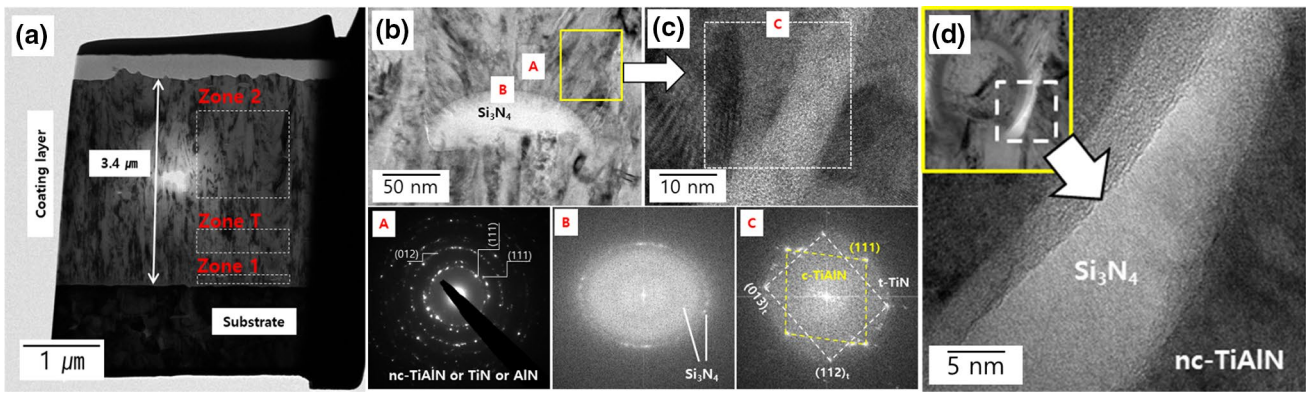

Fig. 5 Microstructures of the $Ti_{50}Al_{45}Si_5N$ coating layer: **a** as-FIBed image, **b** BF image of zone 2 (A, B: SAED patterns), **c** HR-TEM image of enlarged region from **b** with corresponding FFT pattern, and **d** HR-TEM image of zone T in TiN/α-Si_3N_4/TiAlN

in matrix c-(Al, Ti)N_2. Precipitated nitride (i.e. TiN) was embedded at the TiN/Si_3N_4/TiAlN interface, this can be clearly observed by the HR-TEM micrograph shown in Fig. 5d.

Figure 6 shows the $Ti_{45}Al_{45}Si_{10}$ (#2) coating layer micrographs. In Fig. 6a, we can see the thickness of the coating layer deposited is about 2.3 μm. Compared to composition #1, we can see a constant growth direction for the fine nitrides in the T region was presented locally, however the emergence of a columnar crystals were hardly observed in shown Fig. 6b. The preferentially oriented direction of growth induces the formation of dense columnar crystalline structures in zone 2, as shown in Fig. 6c. Their enlarged images (see Fig. 6d) for A, B, and C regions coincide inter-planar spacing of inherent in nitrides by demonstrated experimentally.

Figure 7 shows the micrographs of the $Ti_{40}Al_{45}Si_{15}$ (#3) coating layer. Figure 7a, we can see the thickness of the coating layer deposited is about 3.0 μm, we can also see that Si_3N_4 is concentrated in zones T and 2. That is, we can see the formation of amorphous phase in the Si-rich corner. Also, by referring to the BF image and the diffraction pattern in Fig. 7b, the grain refinement causes an obvious overlapping pattern in the amorphous/crystalline groups, compared to the pattern shown in Fig. 7a. This behavior is consistent with that reported in several studies [20–25], the amorphous phase (i.e. Si_3N_4) acts as an obstacle to growth of the nitride crystalline, which promotes grain refinement. From another

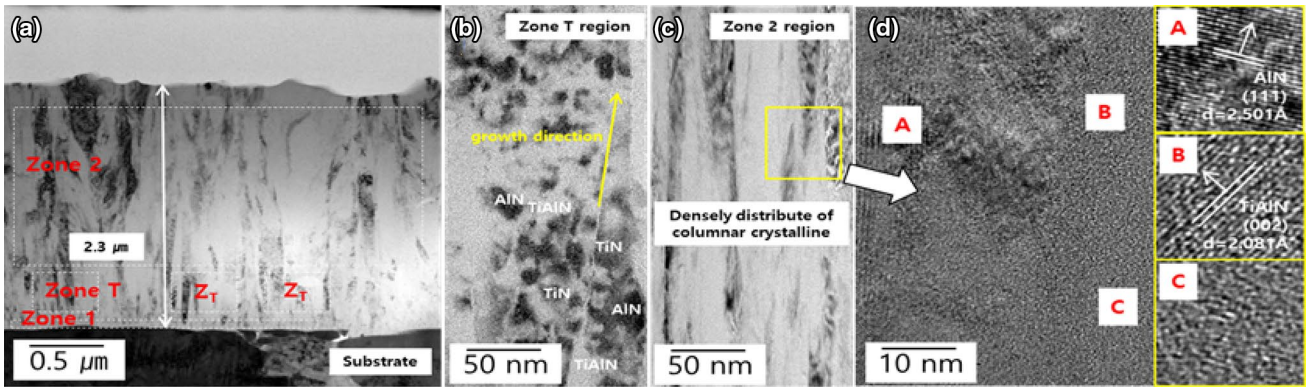

Fig. 6 Microstructures of the $Ti_{45}Al_{45}Si_{10}N$ coating layer: **a** as-FIBed image, **b** and **c** BF images of zone T and 2, and **d** HR-TEM image of enlarged region for **c** with corresponding interplanar spacing

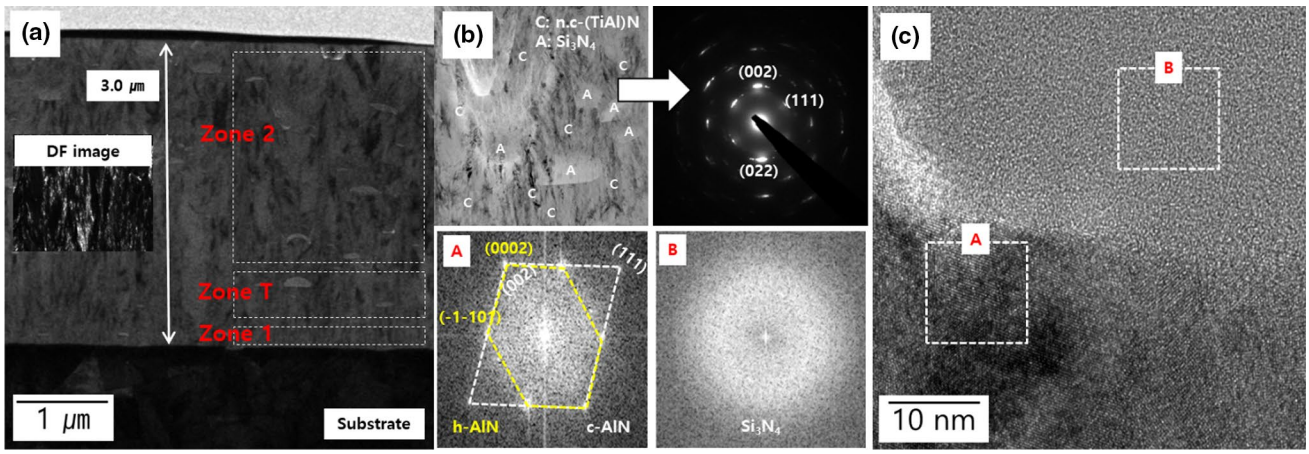

Fig. 7 Microstructures of the $Ti_{40}Al_{45}Si_{15}N$ coating layer: **a** as-FIBed image and corresponding DF image of columnar structure, **b** BF images and SAED patterns of zone 2, and **c** HR-TEM image and corresponding FFT patterns for crystalline(A)/amorphous(B) interface

point of view, grain refinement could be microstructural evidence for the precipitation of fine grains by phase transition in accordance with Al-rich corner. In fact, from FFT pattern of A region in Fig. 7b we can see the sub-lattices h-AlN (h: hexagonal) in matrix c-AlN (c: cubic). Thus, we can see this interaction between the amorphous phase and the fine grain further promotes grain refinement.

To clarify the configuration of nitrides based on their lattice parameter, in Fig. 8 we see the evolution process of the crystal structures drawn by the VESTA software. Additionally, the details of the lattice parameters (e.g. d-spacing, strain energy, and volume of nitrides) are included in the refined XRD data presented in Table 1.

Figure 8a shows the transition of a unit cell of AlN. We can see the distortion of the lattice by the stress field, i.e. it is under tensile σ (t) or compressive σ (c) loads. Decreases in the d-spacing distance due to the distortion in lattice is caused by the compressive stress, increases of this distance are due to tensile stress. Due to h-AlN precipitation in the c-AlN matrix in the Al-rich corner (#3), there is an abrupt decrease of strain energy (i.e. $0.265 \rightarrow 0.191$) in c-AlN and an accompanying increase in volume (i.e. $82.857\ 10^6\ pm^3 \rightarrow 82.956\ 10^6\ pm^3$), this is modeled by Eq. (2).

Figure 8b shows the transition of a unit cell of TiN. It is noteworthy that high strain energy (i.e. 0.509) for c-TiN is only detected in the Ti–rich corner (#1). It could be assumed that it has a relatively unstable structure compared to t-TiN (see the FFT image in Fig. 7c) and it was precipitated from the c-(Al, Ti)N_2 solid solution.

Figure 8c shows the structural evolution of the titanium aluminide nitrides (i.e. $Ti_{1-x}Al_xN$). Crystallographically, the $Ti_{1-x}Al_xN$ coatings have two structures: one is wurtzite (hcp) that has more Al content than Ti; the other is a NaCl-type (fcc) structure which is the opposite in terms of content (i.e. Al < Ti). We presume that precipitates (i.e. c-TiN and h-AlN) from crystal transitions increase the instability of the solid solutions; this could explain their highly deformable strain energies. In other words, it can be assumed that c-(Al, Ti)

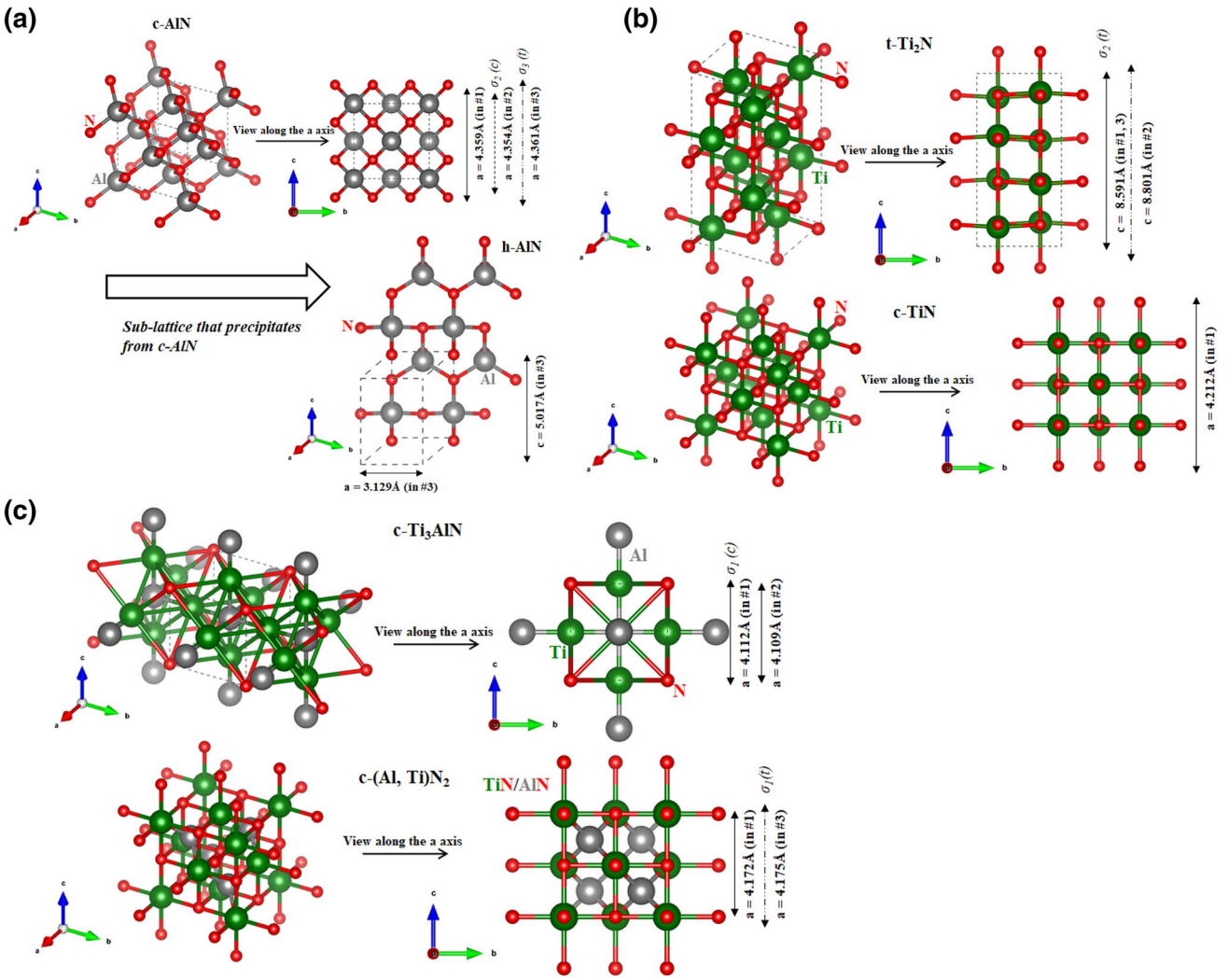

Fig. 8 Constitutive representation of nitride nano-crystalline drawn by the VESTA software with refined XRD data: **a** AlN, **b** TiN, and **c** $Ti_{1-x}Al_xN$

Table 1 Lattice parameters of nitride nano-crystalline structure in TiAlSiN coating layers extracted from Williamson–Hall plot and d-spacing data

Composition	$Ti_{50}Al_{45}Si_5N$ (#1)			$Ti_{45}Al_{45}Si_{10}N$ (#2)			$Ti_{40}Al_{45}Si_{15}N$ (#3)			Index
	d (Å)	Strain (%)	V (10^6 pm^3)	d (Å)	Strain (%)	V (10^6 pm^3)	d (Å)	Strain (%)	V (10^6 pm^3)	
c-AlN	2.517	0.265	82.857	2.514	0.268	82.561 (↓)	2.518	0.191	82.956 (↑)	↑: tensile stress ↓:compressive stress
h-AlN							2.709	0.209	42.527	
t-Ti_2N	1.883	0.190	151.404	1.881	0.199	151.583 (↑)	1.883	0.190	151.404 (↓)	
c-TiN	2.107	0.509	74.831							
c-Ti_3AlN	1.456	0.210	69.530	1.453	0.210	69.411(↓)				
c-(Al, Ti)N_2	2.075	0.504	71.470				2.097	0.678	73.770 (↑)	

N_2 solid solution has instability immediately before spinodal decomposition ($TiAlN_2 \rightarrow TiN + AlN$) [46], which is similar behavior to the aging hardening phenomenon (i.e. a mismatch in the quantum mechanical structure of TiN and AlN) for coating layers. Thus, this behavior could be accelerated by super saturation properties in the alloyed powder (#1) to the compacts (#3). On the other hand, for c-Ti_3AlN the positions of the close-packed atoms correspond with the stacking

sequence ABC–ABC (see #1 and #2). In particular, the Ti^{+} atoms substituting for Al^{+} atoms leads to stronger covalent Ti–Ti and N–Ti bonds [47], which to stable structure within formation energy (Ti_3AlN, −1.020 eV) for additional ionic bonding contributions. Thus, their decomposition behavior (i.e. $Ti_3AlN \rightarrow Ti_2AlN + Ti_3Al + TiN$) could be more stable than that of (Al, Ti)N_2 during the aging hardening process.

The micro hardness of as-deposited the TiAlSiN coatings are shown in Fig. 9 according to the grain size of the nitrides, which were strengthened by increased Si contents. In fact, hardness increased from 41.3 to 45.3 GPa with a decrease in grain size from 48 to 35 nm. The orientation of the propagation of stress to vertical cracks suppressed by collapsing columnar growth (i.e. grain refinement) by forming the amorphous (Si_3N4) in interface nitride crystalline, which accompanied into cohesive energy [20, 21]. Thus, the decrease of crack propagation due to indentation, causing in an strengthened hardness, which coatings of (#3) demonstrated to high hardness by the mutually behaviors with cohesive energy at interface and grain refinement.

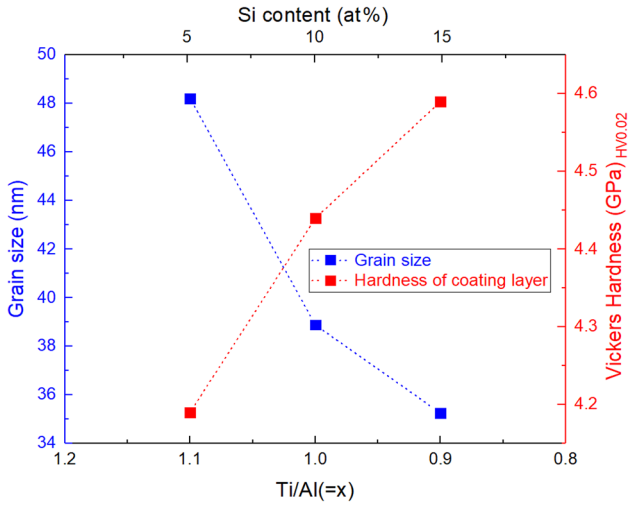

Fig. 9 Variation in hardness and grain size of TiAlSiN coating layers according to Si contents

The surface profiles and their root mean-square (RMS) values are presented in Fig. 10. With increasing Si contents, the RMS value increase continuously with #1: 0.078 μm, #2: 0.098 μm, and #3: 0.104 μm. Cheng et al. reported in [48] that during deposition of a target material with higher Si contents, arc plasma is less stable, which can induce condensate Si rich-phase, i.e. macro-particles. These condensate particles could contribute to a rougher surface that causes an increase in friction coefficient.

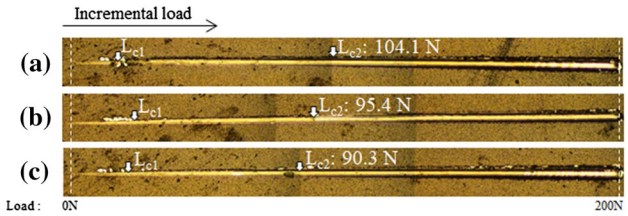

Fig. 11 Micrograph of linear scratches in TiAlSiN coatings: **a** $Ti_{50}Al_{45}Si_5N$, **b** $Ti_{45}Al_{45}Si_{10}N$, and **c** $Ti_{40}Al_{45}Si_{15}N$

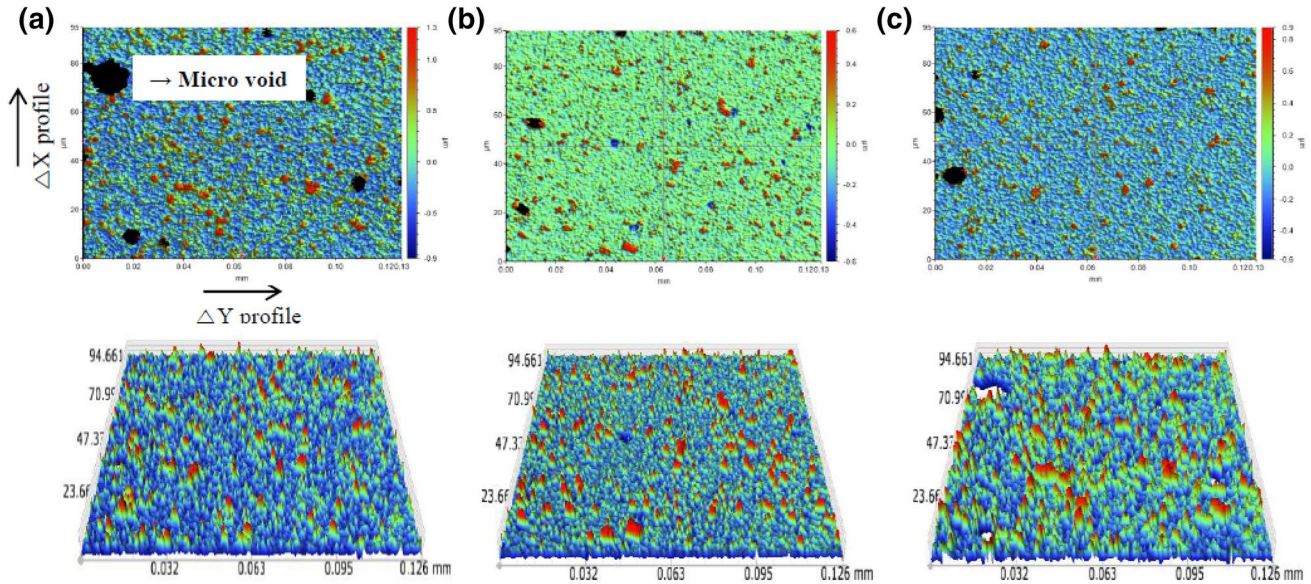

Fig. 10 3D optical profile of TiAlSiN coating layers showing their thickness and morphologies: **a** $Ti_{50}Al_{45}Si_5N$, **b** $Ti_{45}Al_{45}Si_{10}N$, and **c** $Ti_{40}Al_{45}Si_{15}N$

Table 2 Comparison of mechanical properties from several pieces of literature

Coatings	Adhesion (N) or HF degree	Friction coefficient	Hardness (GPa)	Substrate	References
$Ti_{64}Al_{30}Si_6N$	100	–	28.5 ± 31.0	WC–Co	[49]
TiAlSiN	>30	0.05–0.07	48.0	WC–Co	[50]
TiAlSiN	HF 2–HF 5	–	30.0–42.0	WC–Co	[51]
TiAlSiN	67.0 (at Si 9.0 at%)	0.50	40.9	WC–Co	[52]
$Ti_{50}Al_{45}Si_5N$	104.1	0.36	41.3	WC–Co	This study
$Ti_{45}Al_{45}Si_{10}N$	93.3	0.42	42.5		
$Ti_{40}Al_{45}Si_{15}N$	90.3	0.43	45.3		

However, the growth of columnar structures with low Si content (see Fig. 5b) induces the formation of microvoids leading to a heterogeneous roughness of the surface, as shown in Fig. 10a. Consequently, low contents of Si leads to a lower friction coefficient (#1, 0.36) in contrast to high Si contents (#3, 0.43), low Si contents also leads to excellent adhesion properties for these hard coatings. In fact, the adhesion properties for the TiAlSiN coatings are shown in Fig. 11, they were measured to be from 90.3 N (#3, L_{C2}) to 104.1 N (#1, Lc_2), which is superior to those seen in several pieces of literature [49–52] (see Table 2).

4 Conclusion

This works took an experimental approach to explore the crystal structure evolution and mechanical properties of TiAlSiN coatings processed by arc ion plasma and deposited to a substrate.

Three compositions of TiAlSi powder were mechanically alloyed and consolidated by planetary ball milling and rapid sintering; the structural evolution of these compositions depends on the phase states or stability, which is related to the formation energy. Their structural properties were affected by the deposited coating's microstructures that contains nitride that may even be amorphous. The relationship of their quantitative distribution was investigated in terms of chemical binding energy from XPS spectra; the phase transition of the nitrides was examined by looking at the XRD peak profiles. The behavior of between the intermetallic nitrides and others structures (e.g. mono-nitride and amorphous) were investigated by micrograph analysis and tracking their diffraction patterns by means of TEM. Constitutive or configurational representation was drawn with VESTA software. The micro hardness of the TiAlSiN coatings were investigated and it was found that they were strengthened after increasing Si contents due to the effect of grain refinement and the cohesive energy generated from the amorphous/crystalline interface. However, with increasing Si content, the adhesion and roughness of the coatings/substrate was decreased by condensate particles.

Acknowledgements This study has been conducted with the support of the Korea Institute of Industrial Technology (KITECH), Production Industry Leading Core Technology Developement Project (1/4) as the "Development of an on-site facility attached cryogenic machining integrated system (KITECH EO-20-0090)".

References

1. P.H. Mayrhofer, R. Rachbauer, D. Holec, F. Rovere, J.M. Schneider, Compr. Mater. Process. **4**, 355–388 (2014)
2. J.H. Lee, H.K. Park, J.H. Jang, I.H. Oh, Met. Mater. Int. **25**, 268–276 (2019)
3. A. Inspektor, P.A. Salvador, Surf. Coat. Technol. **257**, 138–153 (2014)
4. E. Horvath-Bordon, R. Riedel, A. Zerr, P.F. McMillan, G. Auffermann, Y. Prots, W. Bronger, R. Kniep, P. Kroll, Chem. Soc. Rev. **35**, 987–1014 (2006)
5. J.Z. Kong, P. Xu, Y.Q. Cao, A.D. Li, Q.Z. Wang, F. Zhou, Surf. Coat. Technol. **381**, 125108 (2020)
6. J.H. Hahn, M.A. Abro, X. Xiao, D.B. Lee, Met. Mater. Int. (2020). https://doi.org/10.1007/s12540-020-00665-1
7. L.B. Zhao, N. Lin, X.Q. Han, C. Ma, Z.Y. Wang, Y.H. He, Met. Mater. Int. (2020). https://doi.org/10.1007/s12540-020-00614-y
8. J.-H. Lee, I.-H. Oh, J.-H. Jang, J.-H. Kim, S.-K. Hong, H.-K. Park, Met. Mater. Int. (2020). https://doi.org/10.1007/s12540-020-00618-8
9. S.Y. Lee, S.H. Kim, J. Nanosci. Nanotechnol. **14**(12), 8993–8998 (2014)
10. Y. Iwai, Y. Nanjo, K. Okajaki, M. Tao, E. Sentoku, Tribol. Online **12**(2), 49–57 (2017)
11. B.A. Latella, B.K. Gan, K.E. Davies, D.R. Mckenzie, D.G. Mcculloch, Surf. Coat. Technol. **200**(11), 3605–3611 (2006)
12. L. Fieandt, T. Larsson, E. Lindahl, O. Backe, M. Boman, Surf. Coat. Technol. **334**, 373–383 (2018)
13. J.H. Lee, H.K. Park, J.H. Jang, S.K. Hong, I.H. Oh, J. Alloys Compd. **797**, 612–621 (2019)
14. S.S. Malvajerdi, A.S. Malvajerdi, M. Ghanaatshoar, M. Habibi, H. Jahdi, Sci. Rep. **9**, 19101 (2019)
15. F. Giuliani, C. Ciurea, V. Bhakhri, M. Werchota, L.J. Vandeperre, P.H. Mayrhofer, Thin Solid Films **688**, 137363 (2019)
16. J.L. Endrino, C. Rhammar, A. Gutierrez, R. Gago, D. Horwat, L. Soriano, G. Fox-Rabinovich, D. Martin, Y. Marero, J. Guo, J.E. Rubensson, J. Andersson, Acta Mater. **59**(16), 6287 (2011)
17. G.A. Almyras, D.G. Sangiovanni, K. Sarakinos, Materials **12**(2), 215 (2019)
18. H. Huo, M. Zou, IOP Conf. Ser.: Mater. Sci. Eng. **378**, 012014 (2018)
19. Y.Y. Chang, C.Y. Hsiao, Surf. Coat. Technol. **204**(6–7), 992–996 (2009)

20. I. Endler, M. Hohn, J. Schmidt, S. Scholz, M. Herrmann, M. Knaut, Surf. Coat. Technol. **215**, 133–140 (2013)
21. S. Carvalho, L. Rebouta, A. Cavaleiro, L.A. Rocha, J. Gomes, E. Alves, Thin Solid Films **398**, 391–396 (2001)
22. Y.J. Zhang, Y.Z. Yang, H.W. Ding, Y. Peng, S.M. Zhang, L.G. Yu, P.Y. Zhang, Vacuum **125**, 6–12 (2016)
23. S. Zhang, H.L. Wang, S.E. Ong, D. Sun, X.L. Bui, Plasma Process. Polym. **4**, 219–228 (2007)
24. P.H. Mayrhofer, C. Mitterer, L. Hultman, H. Clemens, Prog. Mater Sci. **51**(8), 1032–1114 (2006)
25. I. Petrov, A. Myers, J.E. Green, J.R. Abelson, J. Vac. Sci. Technol., A **12**(5), 2846–2854 (1994)
26. K. Su, D. Liu, H. Pang, T. Shao, J. Surf, Eng. **34**(7), 504–510 (2018)
27. Y. Liu, H.D. Liu, Q. Wan, Y. Cai, H. Chen, Y.M. Chen, J.J. Guo, B. Yang, J. Surf. Eng. **35**(8), 652–660 (2018)
28. D. Philippon, V. Godinho, P.M. Nagy, M.P. Delplancke-Ogletree, A. Fernandez, Wear **270**(7–8), 541–549 (2011)
29. E. Ribeiro, A. Malczyk, S. Carvalho, L. Rebouta, J.V. Renandes, E. Alves, A.S. Miranda, Surf. Coat. Technol. **151–152**, 515–520 (2002)
30. P. Martin, J. Bendavid, J.M. Cairney, M. Hoffman, Surf. Coat. Technol. **200**, 2228–2235 (2005)
31. D. Rafaja, A. Poklad, V. Klemm, G. Schreiber, D. Heger, M. Sima, M. Dopita, Thin Solid Films **514**, 240–249 (2006)
32. V.D. Mote, Y. Purushotham, B.N. Dole, J. Theor. Appl. Phys. **6**, 1–8 (2012)
33. L.B. McCusker, R.B.V. Dreele, D.E. Cox, D. Louer, P. Scardi, J. Appl. Cryst. **32**, 36–50 (1999)
34. J.R. Tuck, A.M. Korsunsky, D.G. Bhat, S.J. Bull, Surf. Coat. Technol. **139**, 63–74 (2001)
35. M.A. Hassan, A.R. Bushroa, R. Mahmoodian, Surf. Coat. Technol. **277**, 216–221 (2015)
36. I.A. Abrikosov, A. Knutsson, B. Alling, F. Tasnádi, H. Lind, L. Hultman, M. Odén, Materials **4**, 1599–1618 (2011)
37. L. Hultman, Vacuum **57**(1), 1–30 (2000)
38. M. Hans, D. Music, Y.T. Chen, L. Patterer, A.O. Eriksson, D. Kurapov, J. Ramm, M. Arndt, H. Rudigier, J.M. Schneider, Sci. Rep. **7**(1), 1–7 (2017)
39. B. Stannowski, J.K. Rath, R.E.I. Schropp, J. Appl. Phys. **93**(5), 2618 (2003)
40. G. Yu, M.J. Edirisinghe, D.S. Finch, B. Ralph, J. Parrick, J. Eur. Ceram. Soc. **15**(6), 581 (1995)
41. G.M. Ingo, N. Zacchetti, D. della Sala, C. Coluzza, J. Vac. Sci. Technol., A **7**, 3048 (1989)
42. W.H. Chang, I. Bello, W.M. Lau, J. Vac. Sci. Technol., A **11**, 1221 (1993)
43. T.T.T. Hien, C. Ishizaki, K. Ishizaki, J. Ceram. Soc. Jpn. **113**(10), 647–653 (2005)
44. S. Sabooni, F. Karimzadeh, M.H. Abbasi, Bull. Mater. Sci. **35**(3), 439–447 (2012)
45. J. Labar, P. Das, Mircoscopy Microanal. **23**(3), 647–660 (2017)
46. P.W. Shum, K.Y. Li, Z.F. Zhou, Y.G. Shen, Surf. Coat. Technol. **185**(2–3), 245–253 (2004)
47. D. Vogtenhuber-Pawelczak, P. Herzig, J.A. Klima, Z. Phys. B: Condens. Matter **84**, 211–219 (1991)
48. Y.H. Cheng, T. Browne, B. Heckerman, E.I. Meletis, Surf. Coat. Technol. **204**, 2123–2129 (2010)
49. J.K. Chen, C.L. Chang, Y.N. Shieh, K.J. Tsai, B.H. Tsai, Procedia Eng. **36**, 335–340 (2012)
50. T. Chaolakova, V. Chitanov, D. Chaliampalias, L. Kolaklieva, R. Kakanakov, Ch. Bahchedjiev, N. Petkov, Ch. Pashinski, G. Vourlias, N. Vouroutzis, E. Polychroniadis, Y. Wang, E.I. Meletis, J. Nano Res. **27**, 15–24 (2014)
51. Q. Ma, L. Li, Y. Xu, J. Gu, L. Wang, Y. Xu, Appl. Surf. Sci. **392**, 826–833 (2017)
52. S.U. Kang, L. DaMeng, S. TianMin, Sci. China Techol. Sci. **58**, 1682–1688 (2015)